Optimization of a High Work Function Solution Processed Vanadium Oxide Hole-Extracting Layer for Small Molecule and Polymer Organic Photovoltaic Cells

I. Hancox,[†] L. A. Rochford,[†] D. Clare,[†] M. Walker,[‡] J. J. Mudd,[‡] P. Sullivan,[†] S. Schumann,[†] C. F. McConville,[‡] and T. S. Jones*,[†]

[†]Department of Chemistry, University of Warwick, Coventry CV4 7AL, U.K.
[‡]Department of Physics, University of Warwick, Coventry CV4 7AL, U.K.

S *Supporting Information*

ABSTRACT: We report a method of fabricating a high work function, solution processable vanadium oxide ($V_2O_{x(sol)}$) hole-extracting layer. The atmospheric processing conditions of film preparation have a critical influence on the electronic structure and stoichiometry of the $V_2O_{x(sol)}$, with a direct impact on organic photovoltaic (OPV) cell performance. Combined Kelvin probe (KP) and ultraviolet photoemission spectroscopy (UPS) measurements reveal a high work function, n-type character for the thin films, analogous to previously reported thermally evaporated transition metal oxides. Additional states within the band gap of $V_2O_{x(sol)}$ are observed in the UPS spectra and are demonstrated using X-ray photoelectron spectroscopy (XPS) to be due to the substoichiometric nature of $V_2O_{x(sol)}$. The optimized $V_2O_{x(sol)}$ layer performance is compared directly to bare indium−tin oxide (ITO), poly(ethyleneoxythiophene):poly(styrenesulfonate) (PEDOT:PSS), and thermally evaporated molybdenum oxide (MoO_x) interfaces in both small molecule/fullerene and polymer/fullerene structures. OPV cells incorporating $V_2O_{x(sol)}$ are reported to achieve favorable initial cell performance and cell stability attributes.
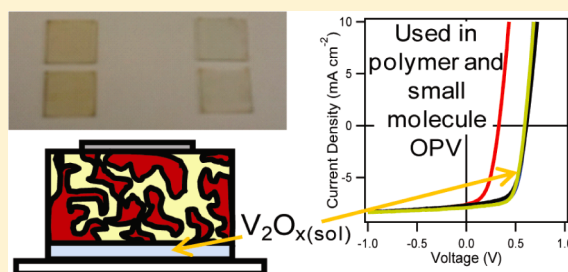
1. INTRODUCTION

Organic photovoltaic (OPV) cells are now near to reaching the power conversion efficiencies (η_p) required for commercialization.[1] Cell performance increases have been due to the development of new active layer materials,[2−5] electrodes, and device architectures.[6−10] The synthesis of donor materials has focused on producing low-band-gap materials to permit increased current generation and the design of high ionization potential materials that allow increases in open circuit voltage (V_{oc}).[11−15] The vast majority of OPV cells still utilize fullerene derivatives as the acceptor material, despite other materials now showing significant potential.[16,17] These donor and acceptor active layers are sandwiched between two electrodes for charge collection. The properties of the electrodes are typically decoupled from the organic materials by the deposition of complementary interfacial charge extracting layers.[18,19]

The use of interfacial layers for modifying the relevant properties of the electrode has been demonstrated to be vital to achieving high cell performance and for increasing cell stability.[20−22] Primarily, poly(ethylenedioxythiophene):poly-(styrenesulfonate) (PEDOT:PSS) has been widely used in the polymer OPV community since it possesses a higher work function than indium−tin oxide (ITO). Consequently, this solution processable layer facilitates higher cell performances than possible with cell fabrication on bare ITO.[23] Despite this improvement, PEDOT:PSS has several drawbacks for use in

commercial cells.[19] These include causing cell degradation due to delamination, etching of the underlying electrode, and electrical inhomogeneity.[19,24−26] Additionally, many of the photoactive organic materials now available possess high ionization potentials in order to obtain large V_{oc} values. Subsequently, higher work function hole-extracting layers are now required to ensure optimal performance due to matching contacts for these materials.

Recently, developments of high work function metal oxide hole-extracting layers have been reported, exhibiting characteristics that enable them to be used as potential alternatives to PEDOT:PSS.[27] Work by Shrotriya et al. revealed the suitability of MoO_x and V_2O_x as hole-extracting layers for the poly(3-hexylthiophene) (P3HT):phenyl-C_{61}-butyric acid methyl ester (PCBM) OPV system.[28] Irwin et al. also demonstrated a significant enhancement of P3HT:PCBM cells by incorporating a p-type nickel oxide (NiO) layer.[25] Further studies of thermally evaporated MoO_x and V_2O_x have revealed the high work function n-type character of the materials.[29−31] The high work function is especially beneficial in cells containing high ionization potential donor materials, such as chloroaluminium phthalocyanine (ClAlPc) and boron subphthalocyanine chlor-

ide (SubPc), reducing losses in V_{oc} and series resistance (R_s).[32,33] In addition, many reports have indicated that incorporating metal oxide layers provides drastically improved cell stability.[32,34] Many different methods of manufacturing the metal oxide layers have been presented, including thermal evaporation, pulsed laser deposition, and solution processing methods.[25,28,35] Solution processed p-type NiO and n-type MoO_x films have achieved comparable performances to layers fabricated by other methods.[35,36] Other novel high work function solution processed layers recently developed include WO_x and nickel acetate.[37,38]

Solution processed metal oxide layers are of great interest due to the low processing costs, compatibility with photoactive blend materials, and the potential for scalability toward commercial production. Recently, Zilberberg et al. demonstrated a solution processed vanadium oxide ($V_2O_{x(sol)}$) layer used in both standard and inverted cell architectures.[39] The layer obtained similar cell performance to both PEDOT:PSS in standard cells and thermally evaporated V_2O_x in inverted cells.[39,40] Interestingly, these layers were fabricated under ambient conditions, despite the majority of OPV active materials available requiring deposition in inert or vacuum conditions.

In this paper, we present data that illustrates the importance of controlling the atmospheric conditions of deposition for solution processed $V_2O_{x(sol)}$ hole-extracting layers. Deposition in ambient conditions is shown to be unfavorable due to a reduced band gap for $V_2O_{x(sol)}$. The yellow discolouration exhibited under ambient conditions does not occur when spin-coating and thermally annealing the layers under N_2. Variations of the layer stoichiometry with fabrication conditions are elucidated using X-ray photoelectron spectroscopy (XPS). The optimal $V_2O_{x(sol)}$ layer is revealed to be a substoichiometric, high work function hole-extracting layer. Direct comparisons of the $V_2O_{x(sol)}$ hole-extracting layer to PEDOT:PSS, thermally evaporated MoO_x, and bare ITO are obtained for both discrete bilayer small molecule and bulk heterojunction polymer/fullerene OPV cells. The $V_2O_{x(sol)}$ hole-extracting layers display remarkable cell performance and significantly increased cell stability compared to the commonly incorporated PEDOT:PSS layers.

2. EXPERIMENTAL SECTION

All cells were fabricated on commercially available ITO-coated glass substrates (Thin Film Devices, 140 nm ITO thickness) after initial solvent cleaning and treatment in ultraviolet/ozone to remove carbon residues. The PEDOT:PSS (Sigma-Aldrich, 1.3 wt % dispersion in water, conductive grade) layers were formed using a filtered (0.45 μm pore size) solution and spin-coated at 6000 rpm, before annealing under ambient conditions at 120 °C for 20 min. Vanadium(V) oxytriisopropoxide (Sigma-Aldrich) was used to fabricate the $V_2O_{x(sol)}$ layers in a 1:40 volume ratio with anhydrous isopropanol (IPA) (Sigma-Aldrich, 99.5%). The solutions were prepared under nitrogen before transfer to the relevant atmospheric conditions, and layers were fabricated immediately in the conditions stated. The solution was spin-coated onto freshly treated ITO at 3000 rpm under stated atmospheric conditions, prior to annealing at 140 °C for 2 min. Bulk heterojunction active layer blends consisted of a 1:1 weight mixture of P3HT (Rieke, >98% regioregular):PCBM (Nano C, >99%), with 20 mg mL^{-1} of each dissolved in anhydrous 1,2-dichlorobenzene (Sigma-Aldrich, 99%). The solution was stirred for 48 h at 40 °C under a N_2

atmosphere. This solution was filtered (0.2 μm pore size) and spin-coated onto substrates at 800 rpm. After drying, the active layers were thermally annealed at 140 °C for 20 min under N_2. The small molecule active layers and MoO_x were grown by thermal evaporation under vacuum in a Kurt J. Lesker Spectros system with a base pressure of 5×10^{-8} mbar. The small molecule materials used, SubPc (Aldrich, 85%) and C_{60} (Nano-C, 99.5%), were purified by thermal gradient sublimation before deposition. MoO_3 (Aldrich, 99.99%) and bathocuproine (BCP, Aldrich) were used as received. A deposition rate of 0.20 nm s^{-1} was used for SubPc, BCP, and MoO_x, with C_{60} grown at 0.05 nm s^{-1}. The aluminum cathodes were deposited in situ by evaporation through a shadow mask, to a thickness of ~100 nm, to give an active cell area of 0.16 cm^2. Where direct comparisons between hole-extracting layers are made, the common layers in all cells within the set were deposited simultaneously to avoid batch-to-batch variations. Current–voltage (J–V) curves were measured using a Keithley 2400 sourcemeter under AM1.5G solar illumination at 100 mW cm^{-2} (1 sun) from a Newport Oriel solar simulator. External quantum efficiency (EQE) measurements were carried out using a Sciencetech SF150 xenon arc lamp and a PTI monochromator, with the monochromatic light intensity calibrated by a Si photodiode (Newport 818-UV). The incoming monochromatic light was chopped at 500 Hz. For signal measurement a Stanford Research Systems SR 830 lock-in amplifier was used. UV/vis electronic absorption spectra were obtained using a PerkinElmer Lambda 25 spectrometer. Ultraviolet photoemission spectroscopy (UPS) measurements were carried out in situ using a custom multichamber ultrahigh vacuum (UHV) system with a base pressure of ~1×10^{-10} mbar. UPS spectra were recorded using a SPECS PHOIBOS 100 hemispherical electron energy analyzer with excitation at 21.21 eV from a He I plasma source. Work function measurements were performed using a Kelvin probe (KP) under a N_2 atmosphere, referenced against freshly cleaved highly ordered pyrolytic graphite. The X-ray photoelectron spectroscopy (XPS) measurements were carried out ex situ after loading into a UHV system with a base pressure of ~5×10^{-11} mbar. The sample was excited with X-rays from a monochromated Al Kα source ($h\nu$ = 1486.6 eV), with the photoelectrons being detected at a 45° takeoff angle using an Omicron Sphera electron analyzer. The combined resolution of the experiment was ~0.5 eV. Atomic force microscopy (AFM) images were obtained from an Asylum Research MFP-3D (Santa Barbara, CA) in ac mode.

3. RESULTS AND DISCUSSION

3.1. Optimization of Solution Processed Vanadium Oxide Hole-Extracting Layers. The impact of the atmospheric conditions for both the spin-coating and annealing processing steps of the $V_2O_{x(sol)}$ layer fabrication were explored. Consequently, four variations of $V_2O_{x(sol)}$ were fabricated, with all combinations of spin-coating and annealing under ambient and N_2 atmospheres produced. Key characteristics when selecting viable hole-extracting layers for OPV cells include good transparency across the visible range of the solar spectra, favorable energetic alignment to the highest occupied molecular orbital (HOMO) of the donor material, and the ability to prevent chemical reactions between active layers and the electrode. All these properties of $V_2O_{x(sol)}$ thin films were considered in order to maximize cell performance.

To be concise, the four different layers distinguished by atmospheric conditions of processing are abbreviated here on in layers spin-coated and annealed under N_2, $V_2O_{x(sol,N2,N2)}$; layers spin-coated under N_2 and annealed in air, $V_2O_{x(sol,N2,air)}$; layers spin-coated in air but annealed under N_2, $V_2O_{x(sol,air,N2)}$; and layers spin-coated and annealed in air, $V_2O_{x(sol,air,air)}$.

Figure 1a illustrates the contrast between $V_2O_{x(sol,air,air)}$ layers (left top and bottom) and $V_2O_{x(sol,N2,air)}$ layers (right top and
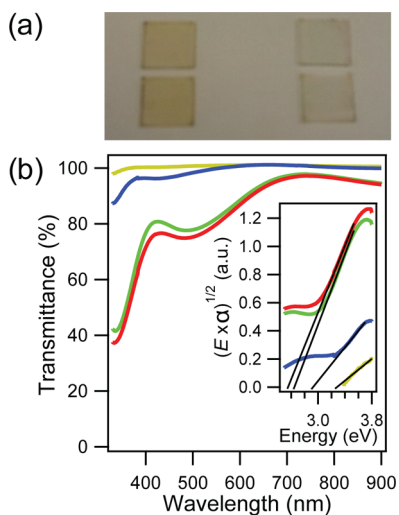

Figure 1. (a) Photograph of $V_2O_{x(sol,air,air)}$ layers (left) and $V_2O_{x(sol,N2,air)}$ layers (right), all on glass/ITO. Two of each are shown to indicate reproducibility. (b) Transmittance of $V_2O_{x(sol,N2,N2)}$ (gold line), $V_2O_{x(sol,N2,air)}$ (blue line), $V_2O_{x(sol,air,N2)}$ (green line), and $V_2O_{x(sol,air,air)}$ (red line). Inset: plot of $(E \times \alpha)^{1/2}$ against energy for each $V_2O_{x(sol)}$ layer.

bottom). When spin-coated in a N_2 atmosphere the $V_2O_{x(sol)}$ layers appear highly transparent with a slight yellow color when viewed at certain angles. However, films processed in ambient conditions have a more noticeable yellow coloration. Changes to the atmospheric conditions during annealing (140 °C, 2 min) do not provide such considerable differences.

The transmittance data in Figure 1b highlight the stark contrast between processing conditions more rigorously. The layers spin-coated in N_2 have similar transmittance profiles, but with a slight decrease from $V_2O_{x(sol,N2,N2)}$ to $V_2O_{x(sol,N2,air)}$. Transmittance is above 97% across the visible range, but below 400 nm the onset of the $V_2O_{x(sol)}$ absorption edge causes considerable reductions. The $V_2O_{x(sol,air,N2)}$ and $V_2O_{x(sol,air,air)}$ layers suffer an extensively reduced transmittance over the entire range. The overall profiles are analogous for layers spun in air, but an additional small loss is encountered when annealing in ambient conditions. Both $V_2O_{x(sol,air,N2)}$ and $V_2O_{x(sol,air,air)}$ layers have reduced transmittance below 700 nm. A broad loss is centered at 480 nm, with reductions of 22% and 25% for $V_2O_{x(sol,air,N2)}$ and $V_2O_{x(sol,air,air)}$ films, respectively.

Interestingly, the onset of the absorption edge is shifted to longer wavelengths with spin-coating in air. In order to estimate the band gap of the $V_2O_{x(sol)}$, a plot of $(E \times \alpha)^{1/2}$ against photon energy is presented in the inset of Figure 1b, where α is absorbance and E is energy in eV.[41] From eq 1 it can be seen that the band gap, E_g, can be obtained from this plot as the intercept of the linear fit at the onset of the $V_2O_{x(sol)}$ valence band absorption with the x-axis.

$$\alpha \propto \frac{1}{E}(E - E_g)^2 \tag{1}$$

The estimation of the band gap of $V_2O_{x(sol)}$ varies with processing conditions. Layers spin-coated under N_2 have band gaps of 3.2 and 2.9 eV for $V_2O_{x(sol,N2,N2)}$ and $V_2O_{x(sol,N2,air)}$ layers, respectively. Spin-coating in ambient conditions produces lower band gaps of 2.6 and 2.5 eV for $V_2O_{x(sol,air,N2)}$ and $V_2O_{x(sol,air,air)}$ films. The reduction of the $V_2O_{x(sol)}$ band gap with processing conditions suggests a possible change of layer stoichiometry.

XPS spectra for each layer are presented in Figure 2. Full survey scans are displayed in the Supporting Information Figure
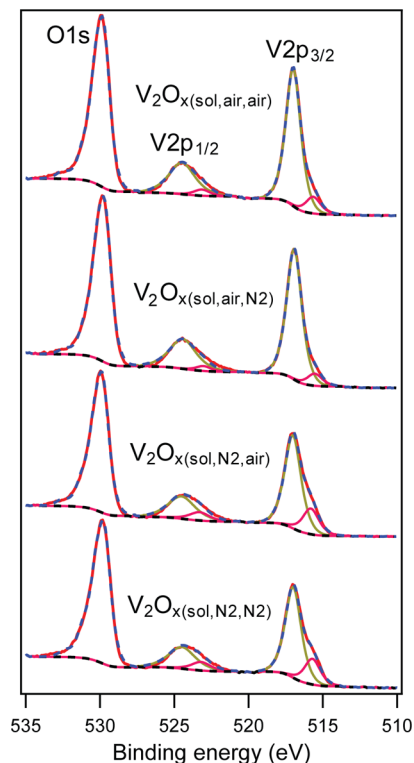

Figure 2. XPS spectra of the V 2p and O 1s region for the $V_2O_{x(sol)}$ layers processed under various conditions. Red lines indicate experimental data, dashed black lines the Shirley backgrounds, and dashed blue lines the fitting envelope, with gold and pink lines representing the major and minor V^{5+} and V^{4+} contributions.

S1. The V 2p peaks obtained exhibit clear asymmetry, with each V 2p region composed of two distinct vanadium oxidation state species. Accordingly, the regions were fitted with a Lorentzian–Gaussian combination to find two separate peaks, consistent with previous literature reports.[39] While each vanadium $2p_{3/2}$ and $2p_{1/2}$ peak invariably demonstrates asymmetry, the extent of the lower binding energy shoulder varied with preparation conditions. Table 1 lists the binding energy for each peak in the V $2p_{3/2}$ region and the relative ratio of the major and minor vanadium oxidation states.

In each case, the dominant vanadium oxidation state peak binding energy was found to be 517.0−516.9 eV. These values are consistent with numerous literature reports for V^{5+}, corresponding to V_2O_5.[30,39,42−44] The features between 1.2 and 1.4 eV lower in binding energy produce peaks centered at 515.8−515.5 eV. Binding energies of V^{4+}, due to VO_2, are commonly reported in this region.[30,42−44] The films spin-

Table 1. Summary of Binding Energy Values for the V^{5+} and V^{4+} Species in the V $2p_{3/2}$ Region, with Determined Relative Ratios of Each under Different $V_2O_{x(sol)}$ Processing Conditions

hole-extracting layer	V^{5+} peak binding energy (eV)	V^{4+} peak binding energy (eV)	diff of binding energy (eV)	$V^{5+}:V^{4+}$
$V_2O_{x(sol,N2,N2)}$	517.0	515.7	1.3	3.5:1
$V_2O_{x(sol,N2,air)}$	517.0	515.8	1.2	3.6:1
$V_2O_{x(sol,air,N2)}$	516.9	515.5	1.4	10.8:1
$V_2O_{x(sol,air,air)}$	517.0	515.6	1.4	8.3:1

coated in ambient conditions produced relative ratios of $V^{5+}:V^{4+}$ of 8.3:1 and 10.8:1 for $V_2O_{x(sol,air,air)}$ and $V_2O_{x(sol,air,N2)}$ layers, respectively. When spin-coated under N_2, there was a clearly reduced overall vanadium stoichiometry, verified by the noticeably more pronounced shoulders in the V 2p region from the V^{4+} oxidation state. Thus, compellingly, the ratio of $V^{5+}:V^{4+}$ is significantly lower with fabrication in N_2, with 3.5:1 and 3.6:1 for $V_2O_{x(sol,N2,N2)}$ to $V_2O_{x(sol,N2,air)}$ layers.

The relative ratios of V^{5+} to V^{4+} with the variation of processing conditions of $V_2O_{x(sol)}$ convincingly correlate with the band gaps obtained from Figure 1. Previous literature reports have studied vanadium oxide layers with lithium and sodium intercalated into the oxide layers, modifying the structure and therefore optical properties of the oxides.[45,46] The intercalation of Na and Li led to partial reductions of the originally stoichiometric V_2O_5 films, analogous to the substoichiometric $V_2O_{x(sol)}$ layers. In stoichiometric V_2O_5, the band gap arises due to the separation of the O 2p valence band and the split V 3d conduction band, thus producing a band gap of ~2.3 eV. Talledo et al. indicated that the intercalation of Li resulted in a partial reduction of the vanadium oxide and consequently in the partial filling of the lower V 3d band.[45] The increased occupation of this band and further reduction of disordered V_2O_5 occurred with additional Li content. Consequently, the reduction of the stoichiometric V_2O_5 resulted in a widening of the band gap from 2.25 to 3.1 eV for the substoichiometric layer. This change of band gap was convincingly rationalized by concluding that in stoichiometric V_2O_5 the optical gap is between the O 2p valence band and the lower V 3d split of the conduction band. However, with intercalation the lower V 3d band is increasingly filled and therefore the band gap widens to be the difference from the O 2p to the upper V 3d band, with a significant difference of energy.[45] Wu et al. indicate a similar reasoning for the change, with reduction of V^{5+} leading to a reduced orbital overlap of the O 2p and V 3d bands, increasing the optical band gap.[46]

Similar arguments for the change of V_2O_5 band gap can be applied here. The $V_2O_{x(sol)}$ layers spin-coated in air produce similar band gaps of 2.5 and 2.6 eV with annealing under ambient and N_2 conditions. These values present band gaps slightly wider than stoichiometric V_2O_5, due to the $V^{5+}:V^{4+}$ ratios presented in Table 1. With significantly increased V^{4+} content due to spin-coating under N_2, the $V_2O_{x(sol)}$ films fabricated according to this process have significantly increased band gaps of 2.9 and 3.2 eV, with annealing in air and N_2. Thus, analogous to the increased intercalation producing wider band gaps, the increased V^{4+} content also results in wider band gaps, acting as a reduced species. Since hole-extracting layers benefit from enhanced transmittance across visible wavelengths, similar layer thicknesses but with increased oxygen deficiency in the

$V_2O_{x(sol)}$ would be expected to facilitate the optimum transmittance for an OPV cell.

Although the change in band gap of $V_2O_{x(sol)}$ thin films can be attributed to stoichiometric changes, the reduced transmittance is expected to correlate with layer thicknesses. AFM step edge measurements (Figure S2) show the $V_2O_{x(sol)}$ fabricated completely under N_2 to be ~5.5 nm thick, while those fabricated in ambient conditions are ~18.2 nm thick. When the layers are spin-coated in air, the solution is likely to undergo a hydrolysis reaction, similar to other metal oxides.[47] This reaction increases the viscosity of the solution and consequently results in thicker layers than those fabricated under N_2 with the same spin-coating parameters.

Despite determining that the layers processed in air are ~3 times thicker than those produced under N_2, this alone cannot account for such a large loss in transmittance at shorter wavelengths. This is demonstrated with the cell data and EQE measurements displayed in the Figure S3 and Table T1. Thus, the combination of favorable stoichiometry, electronic properties, and fabrication of thinner layers under N_2 would suggest an increased suitability of the hole-extracting layers fabricated in this manner for inclusion in OPV cells.

The $V_2O_{x(sol)}$ films were utilized in SubPc/C_{60} discrete bilayer OPV cells, with $J-V$ curves presented in Figure 3. Key
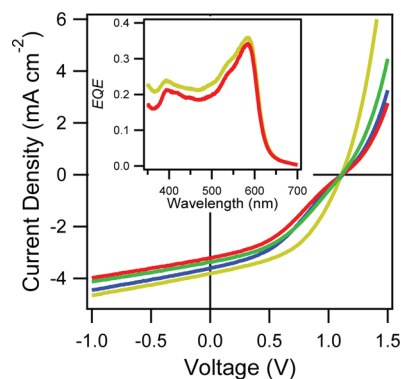

Figure 3. $J-V$ curves obtained under 1 sun illumination for cells with structure ITO/$V_2O_{x(sol)}$/14 nm SubPc/40 nm C_{60}/8 nm BCP/Al, with layers of $V_2O_{x(sol,N2,N2)}$ (gold line), $V_2O_{x(sol,N2,air)}$ (blue line), $V_2O_{x(sol,air,N2)}$ (green line), and $V_2O_{x(sol,air,air)}$ (red line). Inset: EQE measurement of the cells on top of $V_2O_{x(sol,N2,N2)}$ (gold line) and $V_2O_{x(sol,air,air)}$ (red line) hole extracting layers.

cell parameters are summarized in Table 2. The SubPc/C_{60} system was used to compare hole-extracting layers due to the high ionization potential of SubPc.[11,31] This facilitates high V_{oc} values due to a large effective band gap with the C_{60} acceptor and consequently makes the system sensitive to the electronic properties of the hole-extracting layer.[48]

Table 2. Summary of Cell Performance Parameters Obtained with the Architecture ITO/$V_2O_{x(sol)}$/14 nm SubPc/40 nm C_{60}/8 nm BCP/Al, with $V_2O_{x(sol)}$ Processed under Stated Conditions

hole-extracting layer	J_{sc} (mA cm^{-2})	V_{oc} (V)	FF	η_P (%)
$V_2O_{x(sol,N2,N2)}$	3.91	1.12	0.45	2.11
$V_2O_{x(sol,N2,air)}$	3.65	1.12	0.39	1.67
$V_2O_{x(sol,air,N2)}$	3.38	1.10	0.41	1.61
$V_2O_{x(sol,air,air)}$	3.25	1.11	0.38	1.44

As would be expected, the short circuit current density (J_{sc}) decreases by 0.66 mA cm^{-2} when comparing $V_2O_{x(sol,N2,N2)}$ and $V_2O_{x(sol,air,air)}$ layers. This is further demonstrated in the EQE measurement of these cells, shown in the inset of Figure 3. The hole-extracting layers spin-coated in N_2 produce cells with larger J_{sc} values than those spun in ambient conditions. It is evident that fabrication on $V_2O_{x(sol,N2,N2)}$ layers produces cells with a favorable fill factor (FF) value, 0.45. The FF values are reduced to 0.41, 0.39, and 0.38 when cells are deposited onto $V_2O_{x(sol,air,N2)}$, $V_2O_{x(sol,N2,air)}$, and $V_2O_{x(sol,air,air)}$ layers, respectively. The $J-V$ curves in Figure 3 indicate an increase in series resistance (R_s) to be the cause of the losses in FF. Because of the exposure of films to atmospheric conditions, it is likely that water is adsorbed onto the hole-extracting layers surface, causing this detrimental R_s increase.[41]

The V_{oc} values seem to be comparatively unaffected by the processing variations, with cells producing values from 1.10 to 1.12 V. The factors behind this were explored using a KP (under N_2). Utilizing KP allowed a surface sensitive measurement of the work function of the layers without air exposure. The $V_2O_{x(sol)}$ thin films produce remarkably similar work function values, with each in the range 5.6 ± 0.1 eV. Indeed, these work function values are expected to be large enough to cause Fermi level pinning of the SubPc, maximizing each the built-in potential (V_{bi}) of each cell. This is similar to reports for thermally evaporated metal oxides, culminating in the large V_{oc} values obtained.[31,32]

Despite the V_{oc} values achieved, the variation of J_{sc} and FF with $V_2O_{x(sol)}$ processing leads to distinct changes in η_p. The incorporation of $V_2O_{x(sol,N2,N2)}$ layers provided the highest η_p of 2.11%, due to improved transmittance and FF. In direct comparison, cells fabricated on $V_2O_{x(sol,air,air)}$ layers only produced an η_p of 1.44%. The >30% performance loss highlights the significant impact the processing conditions have on $V_2O_{x(sol)}$ layer properties. Thus, the optimal conditions presented here suggest $V_2O_{x(sol)}$ fabrication should be implemented under a N_2 atmosphere.

The high work function of $V_2O_{x(sol,N2,N2)}$ measured by KP indicates the position of the Fermi level. Nevertheless, in order to determine whether $V_2O_{x(sol,N2,N2)}$ is n-type, UPS measurements were acquired. The valence band spectrum and an energy level schematic of the optimized $V_2O_{x(sol,N2,N2)}$ are 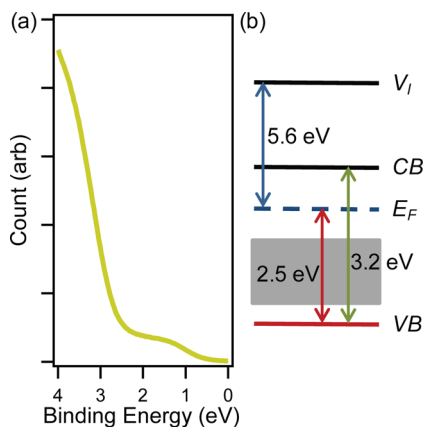shown in Figure 4. The UPS spectrum in Figure 4a reveals the onset of the $V_2O_{x(sol,N2,N2)}$ valence band to be 2.5 eV below the Fermi level. With a band gap estimated earlier to be 3.2 eV, this proves $V_2O_{x(sol,N2,N2)}$ to be highly n-type, as with thermally evaporated MoO_x and V_2O_x.[29−31] Additionally, gap states are displayed within the $V_2O_{x(sol)}$ band gap, between 0.5 and 2.5 eV below the $V_2O_{x(sol,N2,N2)}$ Fermi level. The presence of these additional states should be expected due to the substoichiometric nature of $V_2O_{x(sol,N2,N2)}$ exhibited in XPS. The partial filling of the V 3d lower band is the cause of these additional states, commonly reported for substoichiometric vanadium oxide layers.[42−46] Critically, this compelling experimental evidence verifies that $V_2O_{x(sol,N2,N2)}$ is able to behave in an analogous manner to the thermally evaporated metal oxides previously reported by our group when used as a hole-extracting layer.[31,32,49]

3.2. Direct Comparison of $V_2O_{x(sol,N2,N2)}$ to Commonly Utilized Hole-Extracting Materials.

To determine the relative performance of the $V_2O_{x(sol,N2,N2)}$ layer compared with more commonly used hole-extracting interfaces, sets of both discrete bilayer small molecule and bulk heterojunction polymer/fullerene OPV cells were produced.

Cells with the architecture ITO/(hole-extracting layer)/14 nm SubPc/40 nm C_{60}/8 nm BCP/Al were fabricated, with $J-V$ curves displayed in Figure 5. Key cell parameters are presented
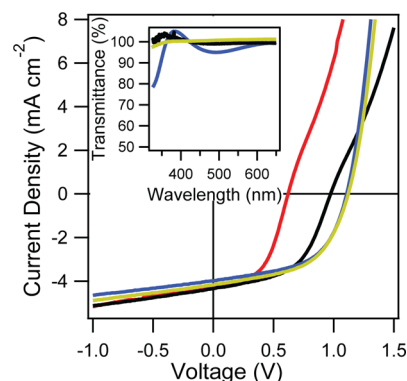
Figure 5. $J-V$ curves obtained under 1 sun illumination for cells with structure ITO/(hole-extracting layer)/14 nm SubPc/40 nm C_{60}/8 nm BCP/Al, where interlayer is ITO (red line), PEDOT:PSS (black line), MoO_x (blue line), and $V_2O_{x(sol,N2,N2)}$ (gold line). Inset: transmittance referenced against an ITO background for each interlayer.

Figure 4. (a) Valence band UPS spectra for $V_2O_{x(sol,N2,N2)}$. (b) Energy level schematic of the optimized $V_2O_{x(sol,N2,N2)}$ constructed from UPS, KP, and UV−vis data (gap states represented by gray box).

Table 3. Summary of Cell Performance Parameters Obtained with the Architecture ITO/(Hole-Extracting Layer)/14 nm SubPc/40 nm C_{60}/8 nm BCP/Al

hole-extracting layer	J_{sc} (mA cm^{-2})	V_{oc} (V)	FF	η_p (%)
ITO	4.24	0.63	0.52	1.34
PEDOT:PSS	4.29	0.97	0.53	2.12
MoO_x	3.98	1.11	0.55	2.33
$V_2O_{x(sol,N2,N2)}$	4.15	1.12	0.53	2.38

in Table 3. The J_{sc} exhibited by the ITO, PEDOT:PSS, and $V_2O_{x(sol,N2,N2)}$ cells gave similar values of 4.24, 4.29, and 4.15 mA cm^{-2}. This correlates well with the transmittance profiles of each layer referenced against an ITO background (Figure 5 inset). While the $V_2O_{x(sol)}$ has marginally preferential transmittance above 425 nm, PEDOT:PSS is more transparent below 425 nm. Accordingly, comparable J_{sc} values should be

expected. MoO_x has a small reduction in J_{sc} compared to ITO, consistent with the reduced transmittance demonstrated for MoO_x, when compared to the other interfaces.[32]

The most striking distinction between the interfaces is demonstrated to be variations in V_{oc}. Both metal oxide layers reveal remarkably high V_{oc} values of 1.11 and 1.12 V for MoO_x and $V_2O_{x(sol,N2,N2)}$, respectively. PEDOT:PSS cells attain a V_{oc} of 0.97 V, with ITO cells only producing 0.63 V. The KP measurement of the PEDOT:PSS surface revealed a work function of 5.3 eV, while the ITO work function was measured at 4.7 eV. This combined V_{oc} and work function data thus adheres to the integer charge model proposed by Crispin et al. and Braun et al.[50,51] This model states that when an organic semiconductor is deposited onto a surface, if the work function energy value of the surface exceeds the integer charge-transfer (ICT) state energy of the organic material, then spontaneous charge transfer occurs, accompanied by Fermi level pinning of the organic to the surface. If the ICT state energy is not exceeded by the surface work function, then no pinning occurs. Here, only hole-extracting layers are varied, therefore focusing on the positive ICT energy (E_{ICT+}), the energy of a relaxed state when one electron is removed and transferred from the organic to the interlayer material, making the E_{ICT+} lower in energy than the HOMO of the material. This elegant model convincingly clarifies the obtained V_{oc} trend of the OPV cells on these interlayers. When the hole-extracting interlayer work function exceeds the E_{ICT+}, the V_{oc} of the cell is maximized and dominated by the effective band gap of the donor and acceptor materials.[52] When the interlayer work function does not exceed the E_{ICT+}, losses in V_{oc} occur, with the V_{oc} proportional to the difference in work function between the electrodes. Since in this work the electron-extracting interface is kept constant throughout, the V_{oc} will linearly depend on the work function of the hole-extracting layer in this situation. With the PEDOT:PSS (work function 5.3 eV) cells obtaining V_{oc} values between that of the metal oxides (work functions 5.6 and 6.4 eV) and ITO (work function 4.7 eV), the interlayers give further evidence of the need for the development of high work function hole-extracting layers. The evident trend of V_{oc} with interface work function additionally suggests the SubPc integer charge transfer state resides between 5.3 and 5.5 eV, as cell V_{oc} is not maximized with the use of a PEDOT:PSS hole-extracting layer.

The cell performance increases from ITO < PEDOT:PSS < MoO_x < $V_2O_{x(sol,N2,N2)}$, with η_p values of 1.34, 2.12, 2.33, and 2.38% obtained, respectively. Despite relatively high J_{sc} values, the ITO and PEDOT:PSS cells show reduced η_p due to the losses in V_{oc}. With comparable η_p and V_{oc} values, MoO_x and $V_2O_{x(sol,N2,N2)}$ are suitable hole-extracting layers for SubPc/C_{60} cells. A marginally higher η_p for the solution processed metal oxide is obtained due to the favorable transmittance.

In order to become more widely applicable, $V_2O_{x(sol,N2,N2)}$ must demonstrate excellent performance with a wide range of cell architectures and active materials. The P3HT:PCBM bulk heterojunction is the most commonly utilized model system by the polymer community, due to relatively high performance, reliable reproducibility, and commercial availability. Consequently, in order to test the feasibility of replacing PEDOT:PSS with $V_2O_{x(sol,N2,N2)}$, P3HT:PCBM cells were also fabricated. ITO and thermally evaporated MoO_x interfaces were also used for comparison to ensure completeness.

It should be noted here that previous reports have successfully used $V_2O_{x(sol,air,air)}$ layers with polymer blends.[39,40]

The solvent used in spin-coating the polymer blend may remove the detrimental adsorbates that cause the increase in R_s and subsequent loss in FF shown in Figure 3. However, since the P3HT:PCBM films are commonly prepared under a N_2 atmosphere and also demonstrated a favorable transmittance profile, it is sensible to prepare the hole extracting layer in the manner used here.

Cells with the architecture ITO/(hole-extracting layer)/P3HT:PCBM/8 nm BCP/Al were fabricated, with the $J-V$ curves shown in Figure 6 and key cell parameters are shown in
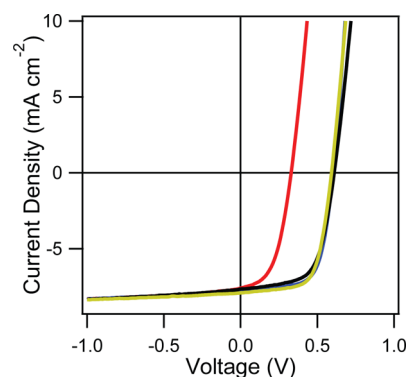

Figure 6. $J-V$ curves obtained under 1 sun illumination for cells with structure ITO/(hole-extracting layer)/P3HT:PCBM/8 nm BCP/Al, where interlayer is ITO (red line), PEDOT:PSS (black line), MoO_x (blue line), and $V_2O_{x(sol,N2,N2)}$ (gold line). Inset: schematic representation of cell architecture.

Table 4. Summary of Cell Performance Parameters Obtained with the Architecture ITO/(Hole-Extracting Layer)/P3HT:PCBM/8 nm BCP/Al

hole-extracting layer	J_{sc} (mA cm^{-2})	V_{oc} (V)	FF	η_p (%)
ITO	7.60	0.33	0.48	1.27
PEDOT:PSS	7.84	0.61	0.62	3.17
MoO_x	7.73	0.60	0.67	3.31
$V_2O_{x(sol,N2,N2)}$	8.13	0.59	0.65	3.34

Table 4. The P3HT:PCBM active layers deposited on bare ITO give a poor η_p of 1.27%. The most striking feature of Figure 6 is the drastically reduced V_{oc} of the ITO cells compared to the hole-extracting layers. With the work function of ITO measured to be 4.7 eV, the cells produce a V_{oc} of 0.33 V. In comparison PEDOT:PSS, $V_2O_{x(sol,N2,N2)}$ and MoO_x achieve comparable values of 0.61, 0.59, and 0.60 V. With the measured work function values of PEDOT:PSS (5.3 eV), $V_2O_{x(sol,N2,N2)}$ (5.6 eV) and MoO_x (6.4 eV) exceeding the P3HT ionization potential (5.2 eV), these layers thus exceed the E_{ICT+} of P3HT and consequently maximize V_{oc}.[47] As with the SubPc/C_{60} cells, the reduced work function of ITO means that it does not exceed the P3HT E_{ICT+} and accordingly produces a lower V_{oc}.

Cells fabricated on $V_2O_{x(sol,N2,N2)}$ and MoO_x obtain high FF values of 0.65 and 0.67. The PEDOT:PSS cells have a marginally lower FF of 0.62 due to a slight increase in R_s. ITO cells suffer a significantly reduced FF of 0.48 in comparison. In the bulk heterojunction cells the compromised built-in field of the cells due to the work function of the ITO interface has a large impact on FF and V_{oc} due to the increased rate of

bimolecular recombination in bulk heterojunctions, compared to discrete bilyer OPV cells.[53]

The PEDOT:PSS and $V_2O_{x(sol,N2,N2)}$ cells achieve J_{sc} values of 7.84 and 8.13 mA cm^{-2}, respectively. The blend deposited on MoO_x produced a slightly reduced J_{sc} of 7.73 mA cm^{-2}. While this is lower than the solution processed metal oxide, the difference is shown to be due to transmittance, as seen for SubPc/C$_{60}$ devices. This is evident in the EQE and transmittance profiles presented for cells containing each hole-extracting layer in Figure S4, clearly indicating the increased current generation for $V_2O_{x(sol,N2,N2)}$ cells, in particular in the range 425−575 nm. The integration of the EQE data between 350 and 750 nm indicates a J_{sc} of 7.13 and 7.31 mA cm^{-2} was produced with the MoO_x and $V_2O_{x(sol,N2,N2)}$ layers, respectively. Further small J_{sc} gains should also be expected with the $V_2O_{x(sol,N2,N2)}$ layer below 350 nm.

P3HT:PCBM cells generate comparable η_p values of 3.17, 3.34, and 3.31% with the incorporation of PEDOT:PSS, $V_2O_{x(sol,N2,N2)}$, and MoO_x hole-extracting layers, respectively. These initial performance values highlight the importance of the hole-extracting layers to achieve high efficiencies. In addition, they suggest the $V_2O_{x(sol,N2,N2)}$ layer has great potential as a solution processed alternative to PEDOT:PSS for polymer and small molecule device systems.

While high initial cell performances are important for measuring the potential promise of a system, cell stability is an equally important factor for OPV cell commercialization. As stated previously, cells fabricated on PEDOT:PSS have been demonstrated to suffer significant degradation. Thermally evaporated MoO_x layers have been shown to significantly enhance the stability of small molecule bilayer OPV cells compared to ITO when subjected to continuous illumination.[32] Zilberberg et al. demonstrated that under storage in air, cells on $V_2O_{x(sol)}$ exhibited far greater stability than fabrication on ITO.[40] Here, cells based on the P3HT:PCBM system on each of the four interfaces was tested over 1 h of constant illumination at 100 mW cm^{-2} AM1.5G under an N$_2$ atmosphere, in order to monitor the relative stability of each interface. The initial "burn in" period of a cell is testing period where the largest losses of cell performance occur.[54,55] The most significant proportional loss of cell stability is likely to be due to the first hour of cell illumination in the burn in period. Reports have shown a linear degradation of performance after the burn in period;[54] however, cells displaying a significant proportional loss of initial performance during the burn in period are of little use for commercial products.

Figure 7 shows the stability of cell η_p, with all the key cell parameters for each hole-extracting layer additionally shown in Table 5 and Figure S5. Cell stability is greatly improved on both metal oxide layers, with 89% and 94% of the starting efficiency retained for $V_2O_{x(sol)}$ and MoO_x based cells. This is in comparison to the 59% and 68% efficiency retention for cells fabricated on ITO and PEDOT:PSS, respectively. Figure S5a,b and Table 5 indicate the improved stability of V_{oc} and J_{sc} for the metal oxide based cells compared to those on ITO and PEDOT:PSS.

The enhanced stability of the $V_2O_{x(sol,N2,N2)}$ as an alternative to PEDOT:PSS provides a further persuasive reason for the inclusion of the metal oxide in polymer/fullerene blend cells. The stability measured for $V_2O_{x(sol,N2,N2)}$ was only marginally lower than that of the thermally evaporated MoO_x layer and a considerable improvement over bare ITO and PEDOT:PSS. Thus, the beneficial stability and similar initial performance
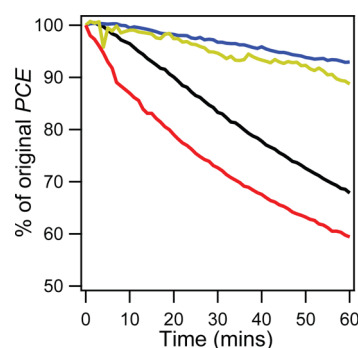

Figure 7. Stability of cell η_p over 60 min constant illumination for the P3HT:PCBM system on each interface, where hole-extracting layer is ITO (red line), PEDOT:PSS (black line), MoO_x (blue line), and $V_2O_{x(sol,N2,N2)}$ (gold line).

Table 5. Summary of Cell Stability Measurements for Each Key Cell Parameter after 1 h Constant Illumination under 1 sun, Displayed as a Percentage of Original Performance[a]

hole-extracting layer	J_{sc} (%)	V_{oc} (%)	FF (%)	η_p (%)
ITO	87	74	93	59
PEDOT:PSS	86	81	97	68
MoO_x	96	97	99	94
$V_2O_{x(sol,N2,N2)}$	92	96	100	89

[a]Measurements were made for the architecture ITO/(interlayer)/P3HT:PCBM/8 nm BCP/Al.

reveal the $V_2O_{x(sol,N2,N2)}$ as a preferential solution processed hole-extracting layer compared to the commonly used PEDOT:PSS layer, when utilized in the P3HT:PCBM system.

4. CONCLUSIONS

In summary, the atmospheric processing conditions of $V_2O_{x(sol)}$ hole-extracting layers were demonstrated to have a significant impact on cell performance. The stoichiometry of $V_2O_{x(sol)}$ layers under each condition was revealed by XPS, with critical changes observed between spin-coating under N$_2$ and in ambient conditions. The transmittance of the layers was compromised by spin-coating in air, due mainly to a reduction of the band gap resulting in a yellow discoloration of layers. The optimal conditions of fabrication were found to be spin-coating and annealing under an N$_2$ atmosphere.

The performance of the optimal $V_2O_{x(sol,N2,N2)}$ layer was directly compared to other common hole-extracting layers, with favorable values achieved. The high work function, measured at 5.6 eV, allowed for analogous performance to thermally evaporated MoO_x hole-extracting layers in discrete bilayer OPV cells utilizing a high ionization potential donor. With this system, cells based on PEDOT:PSS and ITO interfaces produced lower V_{oc} and hence lower η_p. In bulk heterojunction P3HT:PCBM cells, $V_2O_{x(sol,N2,N2)}$ exhibited a similar performance to the commonly used PEDOT:PSS interface but provided greatly improved cell stability. Consequently, the $V_2O_{x(sol,N2,N2)}$ has been shown to be compatible with existing OPV systems and is expected to offer great potential as a solution processed hole-extracting layer with future high ionization potential donor materials in both small molecule and bulk heterojunction device systems.

■ ASSOCIATED CONTENT

S Supporting Information

Supplementary figures showing AFM step edge measurements of the $V_2O_{x(sol)}$ layers, external quantum efficiency measurements of P3HT:PCBM cells on MoO_x and $V_2O_{x(sol,N2,N2)}$ hole-extracting layers, individual key cell performance parameters of the device stability measured over 1 h under constant illumination, and XPS survey scans of each $V_2O_{x(sol)}$ layer. This material is available free of charge via the Internet at http://pubs.acs.org.

■ AUTHOR INFORMATION

Corresponding Author

*E-mail t.s.jones@warwick.ac.uk.

Notes

The authors declare no competing financial interest.

■ ACKNOWLEDGMENTS

■ REFERENCES

(1) http://www.heliatek.com.

(2) Small, C. E.; Chen, S.; Subbiah, J.; Amb, C. M.; Tsang, S.-W.; Lai, T.-H.; Reynolds, J. R.; So, F. Nat. Photonics **2012**, 6, 115−120.

(3) Li, Y. Acc. Chem. Res. **2012**, 45, 723−733.

(4) Huo, L.; Zhang, S.; Guo, X.; Xu, F.; Li, Y.; Hou, J. Angew. Chem., Int. Ed. **2011**, 50, 9697−9702.

(5) Paton, A. S.; Morse, G. E.; Castelino, D.; Bender, T. P. J. Org. Chem. **2012**, 77, 2531−2536.

(6) Schumann, S.; Bon, S. A. F.; Hatton, R. A.; Jones, T. S. Chem. Commun. **2009**, 42, 6478−6480.

(7) Stec, H. M.; Williams, R. J.; Jones, T. S.; Hatton, R. A. Adv. Funct. Mater. **2011**, 21, 1709−1716.

(8) Po, R.; Carbonera, C.; Bernardi, A.; Tinti, F.; Camaioni, N. Sol. Energy Mater. Sol. Cells **2012**, 100, 97−114.

(9) Li, X.; Choy, W. C. H.; Huo, L.; Xie, F.; Sha, W. E. I.; Ding, B.; Guo, X.; Li, Y.; Hou, J.; You, J.; et al. Adv. Mater. **2012**, 24, 3046−3052.

(10) Tan, Z. a.; Zhang, W.; Zhang, Z.; Qian, D.; Huang, Y.; Hou, J.; Li, Y. Adv. Mater. **2012**, 24, 1476−1481.

(11) Mutolo, K. L.; Mayo, E. I.; Rand, B. P.; Forrest, S. R.; Thompson, M. E. J. Am. Chem. Soc. **2006**, 128, 8108−8109.

(12) Nie, W.; Coffin, R. C.; Liu, J.; Li, Y.; Peterson, E. D.; MacNeill, C. M.; Noftle, R. E.; Carroll, D. L. Appl. Phys. Lett. **2012**, 100, 083301.

(13) Yiu, A. T.; Beaujuge, P. M.; Lee, O. P.; Woo, C. H.; Toney, M. F.; Frechet, J. M. J. J. Am. Chem. Soc. **2012**, 134, 2180−2185.

(14) Castrucci, J. S.; Helander, M. G.; Morse, G. E.; Lu, Z.-H.; Yip, C. M.; Bender, T. P. Cryst. Growth Des. **2012**, 12, 1095−1100.

(15) Morse, G. E.; Helander, M. G.; Stanwick, J.; Sauks, J. M.; Paton, A. S.; Lu, Z.-H.; Bender, T. P. J. Phys. Chem. C **2011**, 115, 11709−11718.

(16) Beaumont, N.; Cho, S. W.; Sullivan, P.; Newby, D.; Smith, K. E.; Jones, T. S. Adv. Funct. Mater. **2012**, 22, 561−566.

(17) Sullivan, P.; Duraud, A.; Hancox, I.; Beaumont, N.; Mirri, G.; Tucker, J. H. R.; Hatton, R. A.; Shipman, M.; Jones, T. S. Adv. Energy Mater. **2011**, 1, 352−355.

(18) Schumann, S.; Da Campo, R.; Illy, B.; Cruickshank, A. C.; McLachlan, M. A.; Ryan, M. P.; Riley, D. J.; McComb, D. W.; Jones, T. S. J. Mater. Chem. **2011**, 21, 2381−2386.

(19) Ratcliff, E. L.; Zacher, B.; Armstrong, N. R. J. Phys. Chem. Lett. **2011**, 2, 1337−1350.

(20) Gommans, H.; Verreet, B.; Rand, B. P.; Muller, R.; Poortmans, J.; Heremans, P.; Genoe, J. Adv. Funct. Mater. **2008**, 18, 3686−3691.

(21) Li, J.; Kim, S.; Edington, S.; Nedy, J.; Cho, S.; Lee, K.; Heeger, A. J.; Gupta, M. C.; Yates, J. T., Jr. Sol. Energy Mater. Sol. Cells **2011**, 95, 1123−1130.

(22) Ratcliff, E. L.; Meyer, J.; Steirer, K. X.; Armstrong, N. R.; Olson, D.; Kahn, A. Org. Electron. **2012**, 13, 744−749.

(23) Granstrom, M.; Petritsch, K.; Arias, A. C.; Lux, A.; Andersson, M. R.; Friend, R. H. Nature **1998**, 395, 257−260.

(24) Ratcliff, E. L.; Lee, P. A.; Armstrong, N. R. J. Mater. Chem. **2010**, 20, 2672−2679.

(25) Irwin, M. D.; Buchholz, B.; Hains, A. W.; Chang, R. P. H.; Marks, T. J. Proc. Natl. Acad. Sci. U. S. A. **2008**, 105, 2783−2787.

(26) Girtan, M.; Rusu, M. Sol. Energy Mater. Sol. Cells **2010**, 94, 446−450.

(27) Po, R.; Carbonera, C.; Bernardi, A.; Camaioni, N. Energy Environ. Sci. **2011**, 4, 285−310.

(28) Shrotriya, V.; Li, G.; Yao, Y.; Chu, C. W.; Yang, Y. Appl. Phys. Lett. **2006**, 88, 073508.

(29) Kroeger, M.; Hamwi, S.; Meyer, J.; Riedl, T.; Kowalsky, W.; Kahn, A. Appl. Phys. Lett. **2009**, 95, 123301.

(30) Meyer, J.; Zilberberg, K.; Riedl, T.; Kahn, A. J. Appl. Phys. **2011**, 110, 033710.

(31) Hancox, I.; Rochford, L. A.; Clare, D.; Sullivan, P.; Jones, T. S. Appl. Phys. Lett. **2011**, 99, 013304.

(32) Hancox, I.; Sullivan, P.; Chauhan, K. V.; Beaumont, N.; Rochford, L. A.; Hatton, R. A.; Jones, T. S. Org. Electron. **2010**, 11, 2019−2025.

(33) Kim, D. Y.; Subbiah, J.; Sarasqueta, G.; So, F.; Ding, H. J.; Irfan; Gao, Y. L. Appl. Phys. Lett. **2009**, 95, 3.

(34) Voroshazi, E.; Verreet, B.; Buri, A.; Mueller, R.; Di Nuzzo, D.; Heremans, P. Org. Electron. **2011**, 12, 736−744.

(35) Girotto, C.; Voroshazi, E.; Cheyns, D.; Heremans, P.; Rand, B. P. ACS Appl. Mater. Interfaces **2011**, 3, 3244−3247.

(36) Steirer, K. X.; Ndione, P. F.; Widjonarko, N. E.; Lloyd, M. T.; Meyer, J.; Ratcliff, E. L.; Kahn, A.; Armstrong, N. R.; Curtis, C. J.; Ginley, D. S.; et al. Adv. Energy Mater. **2011**, 1, 813−820.

(37) Tan, Z. a.; Li, L.; Cui, C.; Ding, Y.; Xu, Q.; Li, S.; Qian, D.; Li, Y. J. Phys. Chem. C **2012**, 116, 18626−18632.

(38) Tan, Z. a.; Zhang, W.; Qian, D.; Cui, C.; Xu, Q.; Li, L.; Li, S.; Li, Y. Phys. Chem. Chem. Phys. **2012**, 14, 14217−14223.

(39) Zilberberg, K.; Trost, S.; Meyer, J.; Kahn, A.; Behrendt, A.; Luetzenkirchen-Hecht, D.; Frahm, R.; Riedl, T. Adv. Funct. Mater. **2011**, 21, 4776−4783.

(40) Zilberberg, K.; Trost, S.; Schmidt, H.; Riedl, T. Adv. Energy Mater. **2011**, 1, 377−381.

(41) Gwinner, M. C.; Di Pietro, R.; Vaynzof, Y.; Greenberg, K. J.; Ho, P. K. H.; Friend, R. H.; Sirringhaus, H. Adv. Funct. Mater. **2011**, 21, 1432−1441.

(42) Demeter, M.; Neumann, M.; Reichelt, W. Surf. Sci. **2000**, 454, 41−44.

(43) Mendialdua, J.; Casanova, R.; Barbaux, Y. J. Electron Spectrosc. **1995**, 71, 249−261.

(44) Wu, Q. H.; Thissen, A.; Jaegermann, W.; Liu, M. L. Appl. Surf. Sci. **2004**, 236, 473−478.

(45) Talledo, A.; Granqvist, C. G. J. Appl. Phys. **1995**, 77, 4655−4666.

(46) Wu, Q. H.; Thissen, A.; Jaegermann, W. Solid State Ionics **2004**, 167, 155−163.

(47) Kim, J. Y.; Kim, S. H.; Lee, H. H.; Lee, K.; Ma, W. L.; Gong, X.; Heeger, A. J. Adv. Mater. **2006**, 18, 572−576.

(48) Kulshreshtha, C.; Choi, J. W.; Kim, J.-K.; Jeon, W. S.; Suh, M. C.; Park, Y.; Kwon, J. H. Appl. Phys. Lett. **2011**, 99, 023308.

56

dx.doi.org/10.1021/jp3075767 | J. Phys. Chem. C 2013, 117, 49−57

(49) Hancox, I.; Chauhan, K. V.; Sullivan, P.; Hatton, R. A.; Moshar, A.; Mulcahy, C. P. A.; Jones, T. S. *Energy Environ. Sci* **2010**, *3*, 107−110.

(50) Crispin, A.; Crispin, X.; Fahlman, M.; Berggren, M.; Salaneck, W. R. *Appl. Phys. Lett.* **2006**, *89*, 213503.

(51) Braun, S.; Salaneck, W. R.; Fahlman, M. *Adv. Mater.* **2009**, *21*, 1450−1472.

(52) Steim, R.; Kogler, F. R.; Brabec, C. J. *J. Mater. Chem.* **2010**, *20*, 2499−2512.

(53) Shuttle, C. G.; O'Regan, B.; Ballantyne, A. M.; Nelson, J.; Bradley, D. D. C.; Durrant, J. R. *Phys. Rev. B* **2008**, *78*, 113201.

(54) Peters, C. H.; Sachs-Quintana, I. T.; Kastrop, J. P.; Beaupre, S.; Leclerc, M.; McGehee, M. D. *Adv. Energy Mater.* **2011**, *1*, 491−494.

(55) Reese, M. O.; Morfa, A. J.; White, M. S.; Kopidakis, N.; Shaheen, S. E.; Rumbles, G.; Ginley, D. S. *Sol. Energy Mater. Sol. Cells* **2008**, *92*, 746−752.

57

dx.doi.org/10.1021/jp3075767 | *J. Phys. Chem. C* 2013, 117, 49−57